catalysts

MDPI

Article

Partial Oxidation of Methane over CaO Decorated TiO_2 Nanocatalyst for Syngas Production in a Fixed Bed Reactor

Asif Hussain Khoja [1,*], Ahad Hussain Javed [1], Salman Raza Naqvi [2], Sehar Shakir [1], Israf Ud Din [3], Zafar Arshad [2], Umer Rashid [4], Umair Yaqub Qazi [5] and Nida Naeem [1]

1 U.S.-Pakistan Centre for Advanced Studies in Energy (USPCAS-E), National University of Sciences & Technology (NUST), Sector H-12, Islamabad 44000, Pakistan
2 School of Chemical and Materials Engineering (SCME), National University of Sciences & Technology (NUST), Sector H-12, Islamabad 44000, Pakistan
3 Chemistry Department, College of Science and Humanities, Prince Sattam bin Abdulaziz University, P.O. Box 173, Alkharj 11942, Saudi Arabia
4 Institute of Nanoscience and Nanotechnology (ION2), Universiti Putra Malaysia, Serdang 43400, Selangor, Malaysia
5 Department of Chemistry, College of Science, University of Hafr Al Batin, P.O. Box 1803, Hafr Al Batin 39524, Saudi Arabia
* Correspondence: asif@uspcase.nust.edu.pk

Abstract: Syngas is a valuable entity for downstream liquid fuel production and chemical industries. The efficient production of syngas via catalytic partial oxidation of methane (CPOM) is an important process. In this study, partial oxidation of methane (POM) was carried out using CaO decorated TiO_2 catalysts. The catalysts were synthesized employing the sol-gel method, while the decoration of TiO_2 with CaO was achieved in an aqueous solution by wetness impregnation method. The prepared catalysts were characterized by employing XRD, Raman, TG-DTG, and SEM-EDX for structural and morphological analysis. On testing for POM, at 750 °C the catalysts demonstrate excellent CH_4 conversion of 83.6 and 79.5% for 2% and 3% CaO loaded TiO_2, respectively. While the average H_2/CO ratio for both 2% and 3% CaO loaded TiO_2, 2.25 and 2.28, respectively, remained slightly above the theoretical value (H_2/CO = 2.0) of POM. The improved POM performance is attributed to the optimally loaded CaO on the TiO_2 surface that promotes the reaction where TiO_2 support ensure less agglomerated particles, resulting into a fine distribution of the active catalytic sites.

Keywords: partial oxidation of methane; CaO loaded TiO_2; eggshells; syngas

check for updates

Citation: Khoja, A.H.; Javed, A.H.; Naqvi, S.R.; Shakir, S.; Ud Din, I.; Arshad, Z.; Rashid, U.; Qazi, U.Y.; Naeem, N. Partial Oxidation of Methane over CaO Decorated TiO_2 Nanocatalyst for Syngas Production in a Fixed Bed Reactor. *Catalysts* **2022**, *12*, 1089. https://doi.org/10.3390/catal12101089

Academic Editor: Sónia Carabineiro

Received: 28 July 2022
Accepted: 12 September 2022
Published: 21 September 2022

1. Introduction

Natural gas utilization is an increasing trend due its consumption in the energy sector and its conversion into high value chemicals such as syngas, used in various industrial processes [1–3]. Primarily, syngas was used as an important precursor for downstream liquid fuel production via different methods, including Fischer-Tropsch (FT) method, methanol synthesis, etc. [4,5]. Different routes for CH_4 utilization have been studied influentially in chemical society [6] and a major challenge in the use of methane for obtaining useful products is due to its stable four sigma bonds (ΔH_d = 440 kJ/mol) [7]. The use of potential catalysts is an attractive approach to convert methane into syngas and different reforming techniques have been employed such as; steam methane reforming (SMR) [8,9]; dry methane reforming (DRM) [10–12]; and partial oxidation of methane (POM) [13–15]. Although SMR is a commercialized method for H_2 rich syngas production, its endothermic and energy utilization makes it more challenging [16]. In comparison, DRM, an endothermic and less energy intensive than SMR, is considered an important method for converting CH_4 and CO_2 (greenhouse gases) into a valuable chemical. However, this method encounters low H_2/CO ratio, catalyst deactivation readily due to extreme coke deposition and sintering [17].

In recent years, POM has been extensively studied and investigated for CH_4 conversion as it is a fast and cost-effective method with high CH_4 conversion efficiency, selectivity, and short residence time. It produces a H_2/CO ratio of 2.0 (theoretically) that is more suitable for use in FT synthesis [16,18]. POM proceeds either by a direct or indirect mechanism. In the indirect pathway, CH_4 is converted into CO_2 and steam, followed by its reforming to syngas, while in the direct method, syngas can be produced by CH_4 in a single-step, as suggested by Hickman and Schmidt [19]. An assortment of catalysts have been studied for POM including transition metals, noble metals, and perovskites [20], however, the key challenges of metal sintering, hotspot formation and coke deposition that deactivates the catalyst still remained unresolved [21]. While the noble metals are costly in commercial prospect. Therefore, mixed metal oxides with different support materials have been tested to improve conversion and deter catalyst deactivation [22].

The investigation of metal oxides, zeolites, hydrotalcite and alkaline earth metal oxides have shown high product yield with small catalyst loadings [23,24]. For instance, loading of Ni on La_2O_3 exhibited excellent stability, and enhanced activity owing to the favored metal support interaction. Ni nanoparticles were found highly decorated over La_2O_3 that reduced coke formation [25]. While the loading of Co on Yb_2O_3 also proved an efficient catalysts for POM reaction and showed increased conversion rate and stability [26]. Likewise, perovskite based catalysts have been widely used as metal-supported catalysts and received much attention over the past decades as a result of their high activity and thermal stability in POM reactions [27]. Moreover, carbon nanotubes [28], nanoparticles [29], nanocrystals [30], nanocomposites [31], ceria-zirconia containing catalysts [32], nanoclusters [33], ceramic materials [34], hydrotalcite (HT) catalysts [35] and various other structural materials have been used as strong and powerful precursors for the POM. Conventional catalysts broadly utilized in CH_4 partial oxidation are relatively more expensive as compared to waste derived catalysts. Recently, Co loaded waste derived biomass fly ash (BFA) [36] and Co/CeO_2-BFA [37] were employed for methane decomposition and due to the presence of various oxides (SiO_2, Al_2O_3, Fe_2O_3, etc.), is one of the most competitive products to use as a direct support material to improve physicochemical properties and catalytic activity. CaO is another competitive candidate among waste derived catalyst that can be easily obtained from eggshells. CaO has been broadly studied previously due to its low cost and high catalytic activity [38] and due to its strong basic nature. It has been agreed that the active sites of alkaline earth metal oxides are the surface basic sites, produced by the surface metal ion presence that acts like a Lewis acid (electrophile) and an oxygen ion that behaves like a Bronsted basic site. However, these catalysts ca be deactivated by the poisoning of basic sites due to H_2O adsorption at surface sites [39]. Furthermore, alkaline earth metal oxides have a low surface area [40] that promotes onto the surface metal a support interaction, which is favorable for POM [41]. These issues restricted the utilization of simple and environmentally benign catalysts [42]. To cater for these challenges, CaO was impregnated on different supports to increase active sites, surface area and reduce the poisoning of CaO in the reaction medium. Among various supports, such as alumina, zirconia, zeolites, zinc oxide [41], etc., TiO_2 has been extensively studied as TiO_2 is a reducible metal oxide with several crystal structures, and as such, it also possesses multiple oxidation states with moderate chemical and thermal stability [43]. It is encouraging to use TiO_2 as support due to its competitive cost, occurrence, and nontoxic nature in catalytic reactions [44]. Previously, Ni/TiO_2 has been studied for hydrogen production, however, it suffered from coke deposition [45]. Ru/TiO_2 has also shown a promising conversion of methane to syngas [46,47]. Metal support interaction is more crucial in heterogeneous catalysis and a well-known interaction can be more influential for catalyst stability and activity [48] as TiO_2 with VIII B metals suppresses coke deposition due to well-decorated surfaces for metal deposition and the presence of TiO_2 prevents metal agglomeration by increasing metal active sites [49]. Previous reports on Pt/TiO_2 strongly support this hypothesis [49,50]. Furthermore, different preparatory methods have been developed for TiO_2 synthesis, including continuous reaction [51], precipitation [52], sol-gel [53,54] etc.

Among these, sol-gel has gained more attention as the highly crystalline powder can be synthesized with enhanced purity even at low temperatures. It is also possible to control the stoichiometry and structure of the catalyst at the same time, using a prepared via sol-gel method [55].

This work reports the study of waste-derived CaO loaded TiO_2 catalysts for H_2 rich syngas production via POM reaction. The sol-gel method was followed to obtain well defined TiO_2 nanostructures, and eggshells-derived CaO loading over TiO_2 nanostructures was carried out via wetness impregnation route. The synthesized catalysts were characterized by X-ray diffraction (XRD), Raman spectroscopy, Fourier-transform infrared spectroscopy (FTIR), thermogravimetric-differential thermal gravimetric (TGA-DTG), scanning electron microscopy (SEM), and energy-dispersive X-ray spectroscopy (EDX) for structural, stability, morphological and elemental analysis. The influence of different CaO loadings on TiO_2 was progressively studied to obtain an optimum loading. CaO, being basic in nature, can provide more oxygen vacancies to improve the conversion efficiency of TiO_2 and can prevent cooking to avoid the catalyst deactivation. As we know that more oxygen vacancies are responsible for weakening and destabilizing the metal oxygen bonds in TiO_2, which can help to reduce the TiO_2 into metallic phase, so, this study is conducted to find an optimum loading of CaO over TiO_2 showing the most conversion efficiency, as well as stability of the catalyst. Finally, the spent of the catalyst was collected and characterized by Raman and SEM/EDS to study carbon deposition on the catalyst surface.

2. Results and Discussion

2.1. Physicochemical Properties of the Catalyst

XRD patterns of different catalysts are given in Figure 1. The diffraction peaks of 1–3% CaO-TiO_2 and pure TiO_2 powder demonstrated the tetragonal arrangement of TiO_2 anatase phase with (I41/amd(141)) space group and are in good agreement with JCPDS 21-1272 data card peaks [56]. Its major peaks are detected at 2θ = 25.3°, 38.6°, 48°, 53.9°, 55°, and 62.7° with indices (*hkl*) values of (101), (112), (200), (105), (211), and (204) having a dominant peak at (101) (one of the more stable facets having high coordinate Ti) indicating the growth of TiO_2 along c-axis. No additional characteristic peak is observed, showing that prepared samples are free from impurities and pure anatase phase of TiO_2 is obtained without rutile or brookite phase [57]. Moreover, the peak sharpening is observed due to impregnation of CaO. Change in intensity is also noted in CaO impregnated TiO_2, likely due to the metal oxide and support interaction. Moreover, a small peak at 20.39° is observed, indicating the formation of calcium titanium oxide ($CaTi_4O_9$). No distinct peak for CaO is observed due to the low concentration of CaO in doped TiO_2 [58]. Moreover, no shift in diffraction lines of TiO_2 with the increase in CaO content can be possibly due to metal oxide metal interaction instead of substitution of Ti sites with Ca. Crystallite size of TiO_2, 1% CaO-TiO_2, 2% CaO-TiO_2, and 3% CaO-TiO_2 is 12 nm, 21 nm, 19 nm, and 17 nm, calculated using the Scherrer equation [59]. The change in crystallite size is attributed to CaO loading, which may help to improve the crystallinity of titania.

The Raman spectrum is further used for the phase and structural identification of pure and impregnated TiO_2 catalysts. As is shown in Figure 2, three characteristic vibrational modes of TiO_2 are observed at 395, 512, and 640 cm^{-1} with symmetries of B_{1g}, A_{1g}/B_{1g}, and E_g, respectively, clearly indicating the existence of anatase phase and no additional peak for rutile or brookite phase is detected [60,61]. Thus, the results are in good agreement with XRD results. Moreover, CaO impregnated TiO_2 (1–3%) does not present any peak shifts while intensity and broadness were affected by the concentration and impregnation of metal. The peak shifting strongly depends on the number of impurity defects while in (1–3%) CaO impregnated TiO_2 concentration of impurities is low, thus no shifting was observed [62]. Only minor changes were observed in the symmetry of TiO_2 due to lattice distortion generated due to defects with CaO substitution [63], where change in intensities supports CaO loading. All the peaks of CaO loaded TiO_2 samples show a significant

increase in intensities with an increase in the concentration of CaO loading that support the results obtained in XRD patterns.

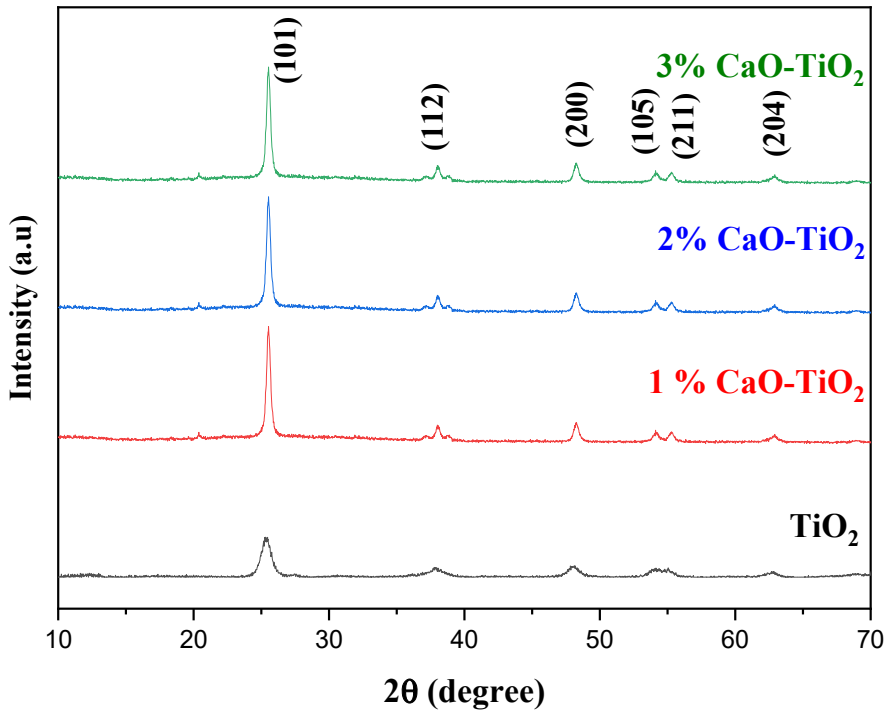

Figure 1. XRD pattern of unloaded TiO_2 and 1–3% CaO loaded TiO_2.

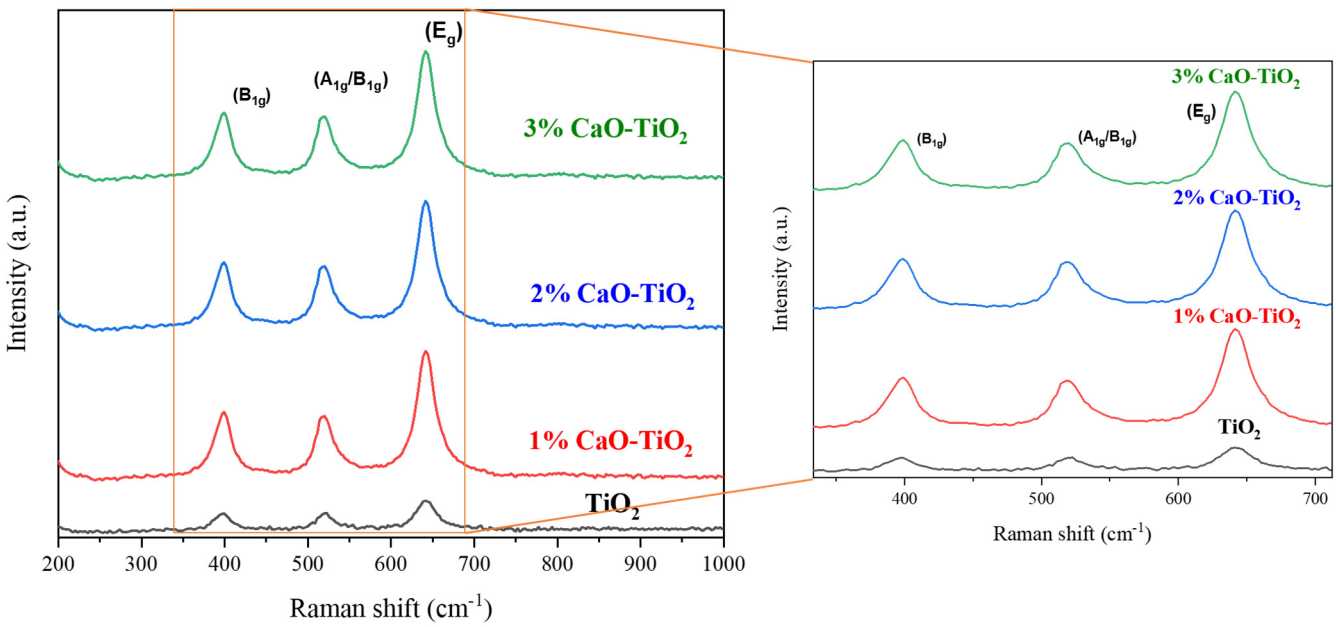

Figure 2. Raman spectroscopy of pure TiO_2 and 1–3% CaO loaded TiO_2.

FTIR spectra of undoped and CaO doped titania is presented in Figure 3a–d. The spectrum is in the range of 600 and 4000 cm^{-1}. In Figure 3a, the peaks at 3200–3600 cm^{-1} are due to OH bonds. In Figure 3c, the intensity of peak around 1200 cm^{-1} and around 2200 cm^{-1} is increased due to the addition of CaO content into the titania lattice. From Figure 3b–d, the intensity of these situated peaks reduces by increasing the amount of the CaO. In Figure 3c, bending vibration is up to a maximum, which is then again reduced when

doped with 3% CaO loaded TiO_2, as shown in Figure 3d. This supports the assumption that 2% loading is an optimized loading. There are some broad peaks at ~ 3600 cm^{-1} then 3100 cm^{-1} indicating the presence of a hydroxyl group, while peaks around 1630 cm^{-1} are found to be corresponding to the bending vibration of H-O-H [64]. The peak near 1140 cm^{-1} corresponds to the possible interaction of the Ti-O-Ca bond. In addition, varying intensity of vibration of the hydroxyl group with increasing doping of up to 2% CaO loading, and then suppression with 3% CaO loading, indicate the presence of various polarities on the effective doping of CaO into the titania lattice, resulting in an increased number of oxygen vacancies with increasing loading up to 2% CaO loading and decreased for 3% CaO loaded TiO_2 [65]. Overall, all the grown catalysts follow the same pattern and indicate 2% CaO loading is an optimized loading and confirm the successful synthesis of desired catalysts as observed in XRD analysis.

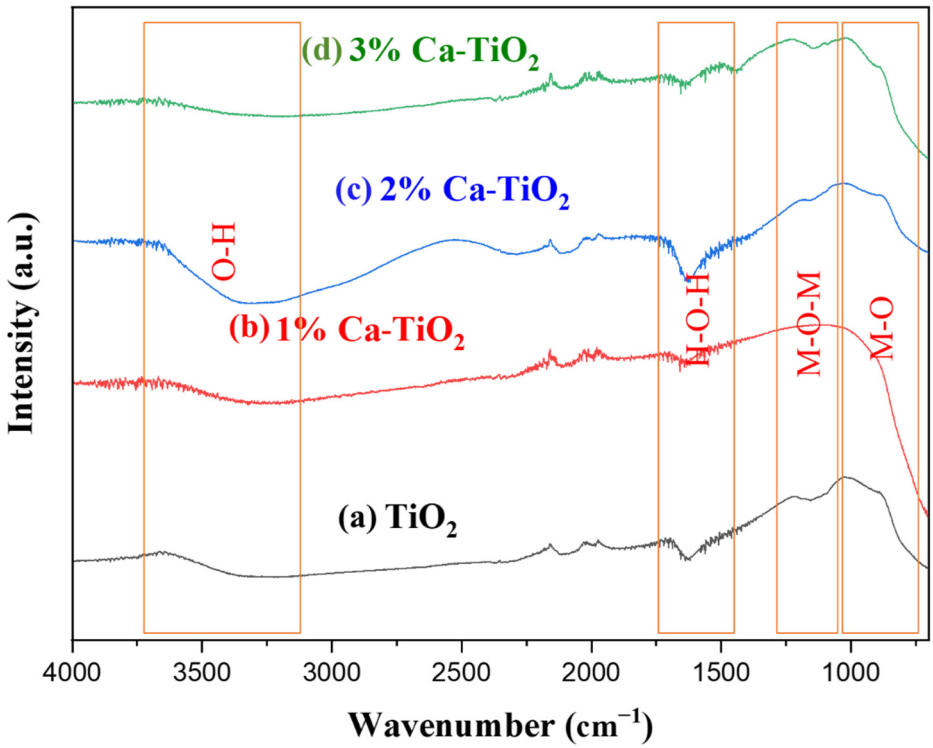

Figure 3. FTIR spectra of (**a**) pristine TiO_2 (**b**–**d**) 1–3% CaO loaded TiO_2.

The thermal stability of synthesized materials was confirmed by TG analysis. It is shown in Figure 4 that pristine and CaO impregnated TiO_2 illustrated major weight loss in the same zone. However, the amount of weight loss was insignificant for both catalysts. The weight loss is further divided into three different zones for more clarity. First, weight loss in the range of 0–125 °C was related to the removal of moisture [66]. Second, weight loss (125–400 °C) was attributed to the loss of hydroxyl groups and the decomposition of different layers of amorphous carbon [67], while the third zone in the range of 400–790 °C was related to the decomposition of any organic impurity and condensation of TiO_2 anatase phases [68]. A total of 4.5% weight loss is observed for pristine titania powder, while 2.5% is observed in the case of doped titania. The thermal stability of CaO loaded catalysts is likely due to the better metal support interaction as proposed in R7 in the reaction mechanism section. Further high coordinate TiO_2 facet 101 on interaction with support CaO can provide more oxygen vacancies that possibly limit the thermal degradation [69]. From the curves of the DTA, a high magnitude of the sharp exothermic response on both Figure 4a,b can be observed. The exothermic temperature was 399 °C in case of undoped Titania, which was reduced to 310 °C for doped Titania. While an earlier phase transformation, from the amorphous to crystalline, in the case of CaO doped titania as compared to pure titania is

observed [70]. These results correspond highly with XRD results as samples are highly crystalline which are thermally stable at high temperatures. The substitution of CaO into the Titania lattice lowers its temperature of crystallization [70,71], and this likely attributes to the thermal stability of doped TiO_2 due to metal impregnation.

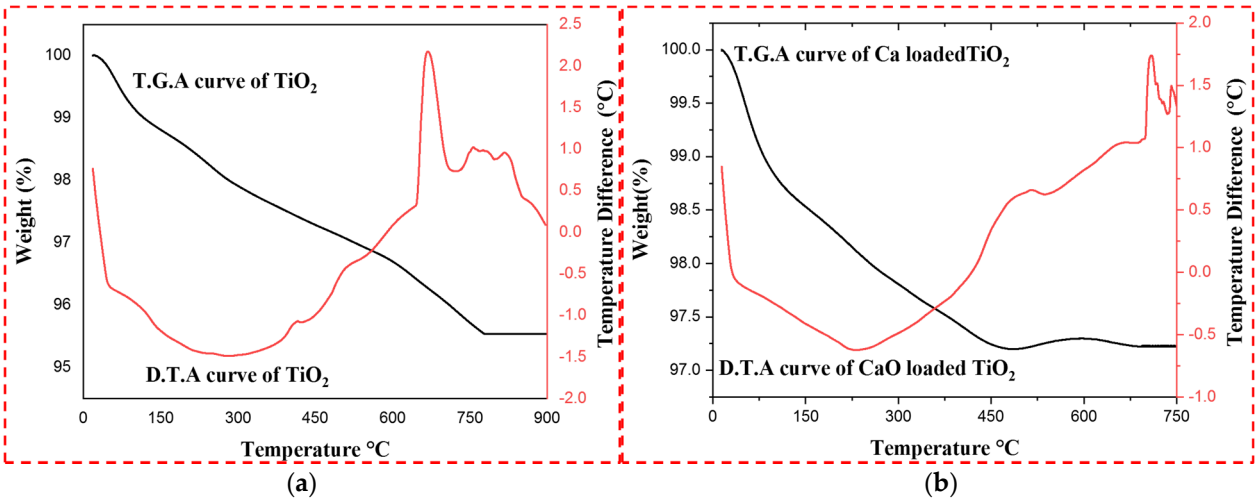

Figure 4. TGA-DTG analysis of (**a**) TiO_2 (**b**) 2% CaO-TiO_2.

The surface morphology of pure and CaO impregnated TiO_2 was characterized by SEM analysis. Figure 5a depicts a very closely packed spherical and well-dispersed bubble-shaped nanostructure of pure TiO_2 [72]. Less agglomeration and well dispersion were due to the aggregation of TiO_2 nanoparticles at high calcination temperature that was more influential for crystalline growth [73]. Surface structure was changed after CaO impregnation, and more uniform and homogenous distribution with irregular spherical morphological agglomeration was attained, as shown in Figure 5b. Thus, SEM analysis demonstrated the difference in morphology between TiO_2 and CaO-TiO_2 [74].

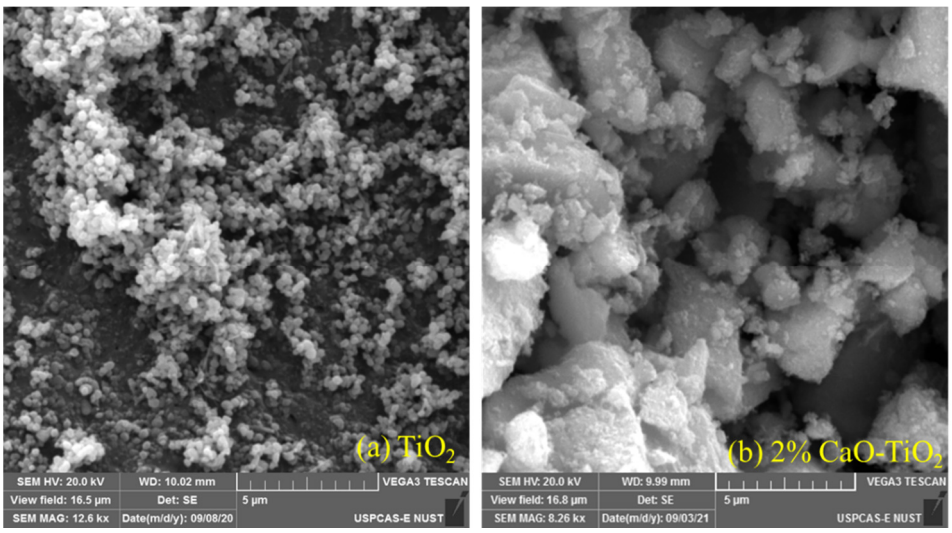

Figure 5. SEM micrographs of (**a**) TiO_2 (**b**) 2% CaO-TiO_2.

In addition to morphological study, the elemental mapping of TiO_2 and CaO-TiO_2 was performed by EDX analysis, and its results are represented in Figure 6. The two intense peaks in Figure 6a represent O (65.90%) and Ti (31.10%) elements, and, 0.39% by weight Ca loading was also detected during analysis represented in Figure 6b that confirmed the presence of CaO in synthesized material, for which no extra characteristic peak and peak

shifting was observed in XRD and Raman spectroscopy due to low metal loading that could only be attributed to a change in intensities.

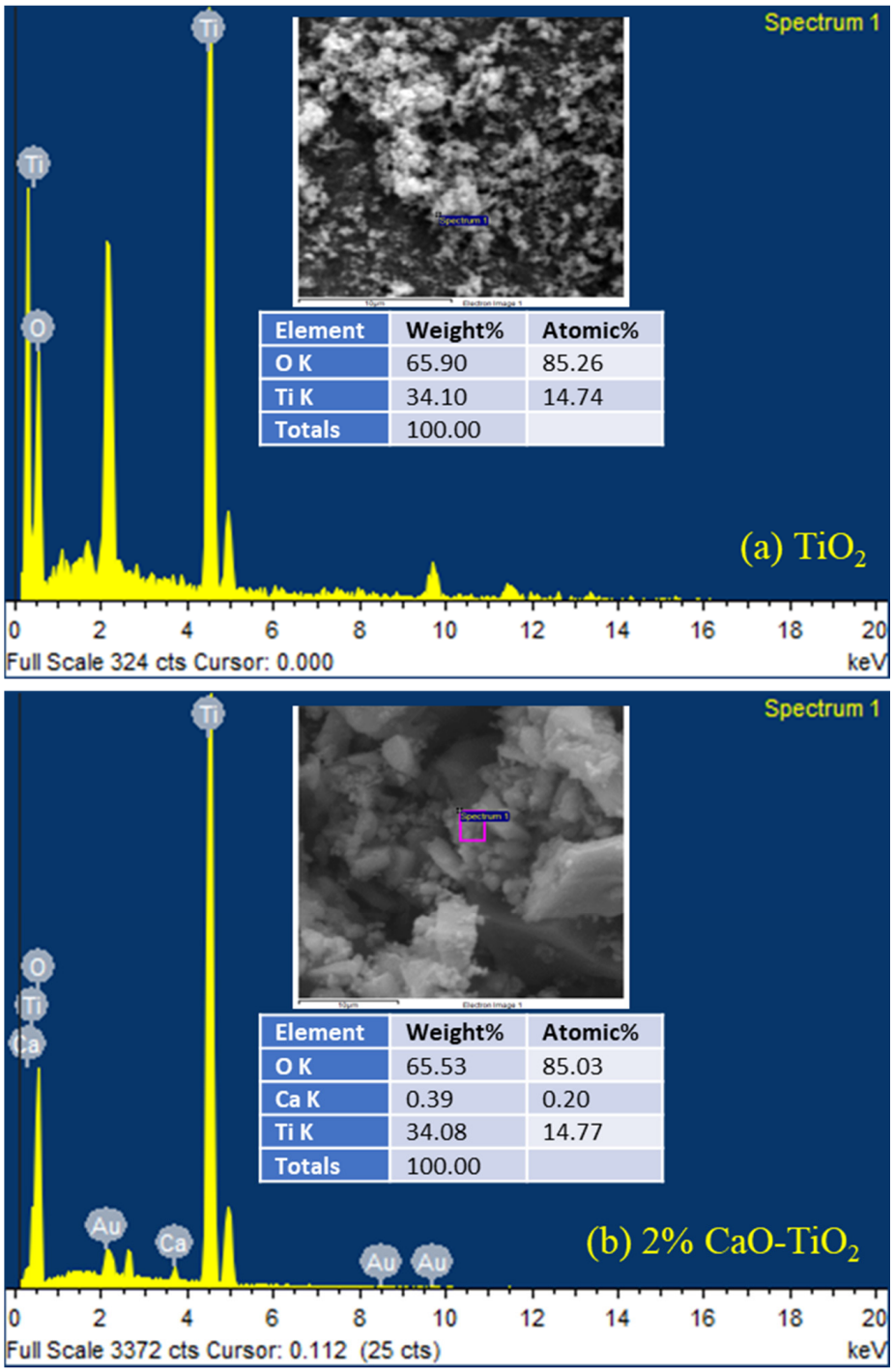

Figure 6. EDX analysis of (**a**) TiO_2 (**b**) 2% CaO-TiO_2.

2.2. Catalyst Performance Analysis

The synthesized catalysts were tested for POM and depicted in Figure 7a–d. The catalysts were allowed to be activated for two hours before sampling. The average of each three readings is taken and used for plots to minimize the error. TiO_2 and CaO loaded TiO_2 showed a smooth and stable trend of conversion on time of the stream. Apart from the trend, an increase in conversion was observed with the CaO loading. However, 2 and 3% CaO loaded TiO_2 have shown almost the same conversion, and a very small change

in conversion is observed after 2% loading for the same amount of loading, assuming 2% is an optimized loading. CaO loading on the surface of TiO_2 support resulted in an active phase exposed for the catalytic reaction [75] due to the combination of earth metal oxide (CaO) and a metal oxide with higher basicity (TiO_2) [76]. An active exposed phase increase with an increase in loading prevents the catalyst from coking and activating the oxidation [77,78], consequently enhancing the conversion efficiency. Furthermore, the activity of CaO on TiO_2 support is related to the increased porosity and oxygen vacancies, resulting in more active sites due to the reduction in metal oxide into a metallic state with an optimal loading [79] at higher temperatures in a hydrogen environment. All the trends for CH_4 conversion (X_{CH4}), selectivity of H_2 (S_{H2}), selectivity of CO (S_{co}), and H_2/CO ratio under experimental conditions reaction temperature =750 °C and flow rate CH_4 = 20 mL min^{-1} O_2 = 10 mL min^{-1} and N_2 = 10 mL min^{-1} are shown in Figure 7. Where CH_4 conversion (X_{CH4}) for 5 h is shown in Figure 7a and an average for 2 and 3% CaO loaded $TiO_2$was approximately 83.56 and 79.54%, respectively. Figure 7b–d illustrate the selectivity of H_2 production, selectivity of CO, and H_2/CO ratio. Selectivity of CO for pristine and 1–3% CaO loaded TiO_2 is almost the same as shown in Figure 7c, however, among all the catalysts, 1% CaO loaded TiO_2 have shown the lowest CO selectivity, likely due to the low concentration of CaO as observed in FTIR analysis. After activation, all the catalysts have shown a stable trend, and not much variation has been observed.

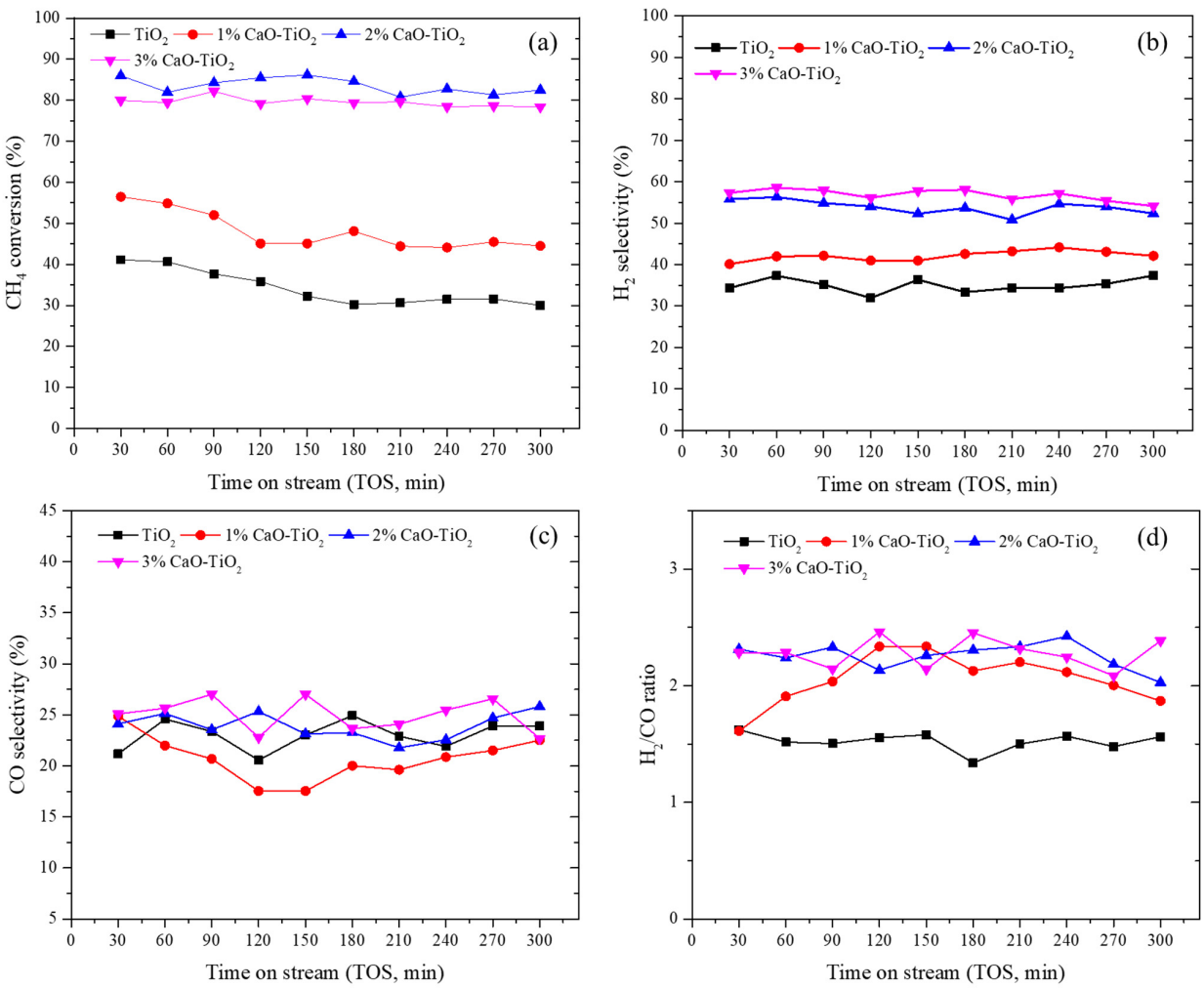

Figure 7. Catalyst stability performance: (**a**) CH_4 conversion; (**b**) H_2 selectivity; (**c**) CO selectivity; (**d**) H_2/CO ratio; catalyst loading 0.2 g, reaction temperature, 750 °C, input ratio 40 mL/min (CH_4 = 20 mL/min, O_2 = 10 mL/min and N_2 = 10 mL/min).

The H_2/CO ratio is also an important parameter in POM, and the H_2/CO ratio for all the catalysts has shown slightly higher values than the stochiometric value, which is 2.0 [80], except TiO_2, which has shown a slightly lower value than the stoichiometric value. The variation in H_2/CO ratio could be evidence of incomplete conversion of CO_2 or a side reaction using CO [81] that may oxidize into CO_2. However, CO_2 can be dissociated into CO due to the presence of anatase phase of TiO_2, as observed in XRD that have a lower energy barrier than rutile phase [82]. However, during CO_2 formation, adsorbed oxygen atoms are consumed resulting in more active sites due to oxygen vacancies. More exposed active sites attributed to CH_4 adsorption, consequently increasing H^* ions that are responsible for an enhanced H_2 production [82,83], which is likely the reason for the higher H_2/CO ratio. The average value of H_2/CO for 2 and 3% CaO loaded TiO_2 was 2.25 and 2.28, respectively, which is slightly above the theoretical value for POM. CaO, which is used as promoter, is highly basic in nature when loaded over TiO_2 101 high coordinate facet, providing more oxygen vacancies that results in an enhanced catalytic activity and hinders coke formation. In addition, the basic character of CaO is further increased the adsorption and prevent the coking consequently activating the oxidizing agent for gasification of carbon. More oxygen vacancies in a result of CaO loading on TiO_2 high coordinate 101 facet are responsible to weaken and destabilize the metal oxygen bond in TiO_2 resulting in the formation of metallic phase during POM reaction at high temperatures such as 750 °C [69]. Highly reduced Ti during POM in a hydrogen environment at high temperature possibly created a synergetic effect resulting in a more stable catalyst and enhanced conversion efficiency.

2.3. Characterization of Spent Catalyst

Spent confirmation is carried out by using Raman spectroscopy as presented in Figure 8, which demonstrates two additional peaks around 1330 (cm^{-1}) and 1580 (cm^{-1}) along with the peaks of pristine CaO loaded TiO_2 confirming the presence of carbon. Moreover, the peak broadening and shifting also support the argument that carbon has been deposited during time on stream. The peak being around 1330 (cm^{-1}) (D Band) validated the existence of disordered graphitic carbon [84,85], though the peak being around 1580 (cm^{-1}) (G Band) is an illustration associated to the ordered graphitic carbon.

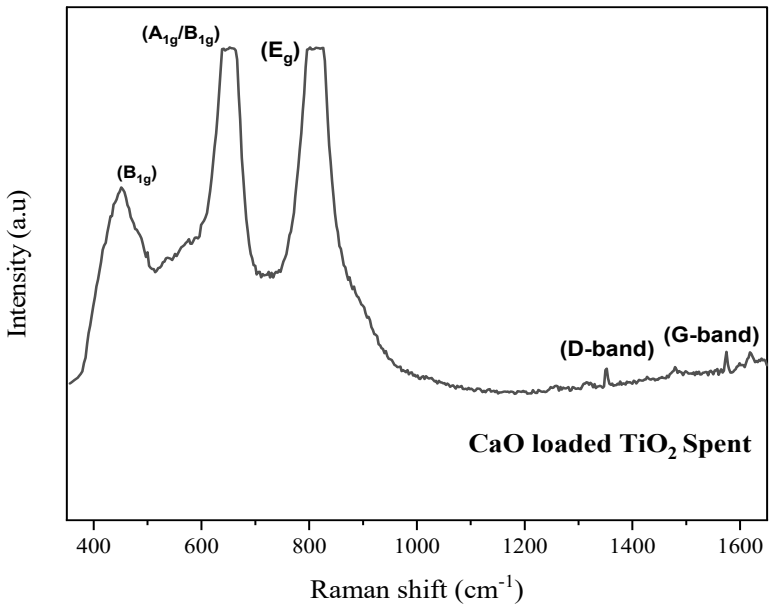

Figure 8. Raman spectra of CaO loaded TiO_2 spent.

Furthermore, SEM/EDX was used for the characterization of the spent catalyst to assess the morphological changes and elemental composition. An SEM micrograph of CaO-TiO_2 spent catalyst is presented in Figure 9a and morphological changes can be seen

in comparison to the fresh catalyst, likely due to the carbon deposition on the surface of catalysts and exposure to high temperature. In addition, morphological changes can also be associated to metal oxide, and uncover atoms which may be present in a different form of adsorbed oxygen along with Ca^{2+} and Ti^{2+} ions, where uncovered oxygen atoms are responsible for H^{+} abstraction and Ca^{2+} and Ti^{2+} ions for C^{-} from the molecule of high acidity (CH_4) [86]. Further EDX spectrum presented in Figure 9b also confirmed the presence of carbon, an intense carbon peak with 3.25% by weight was observed in the EDX spectrum along with Ti and O_2 peaks.

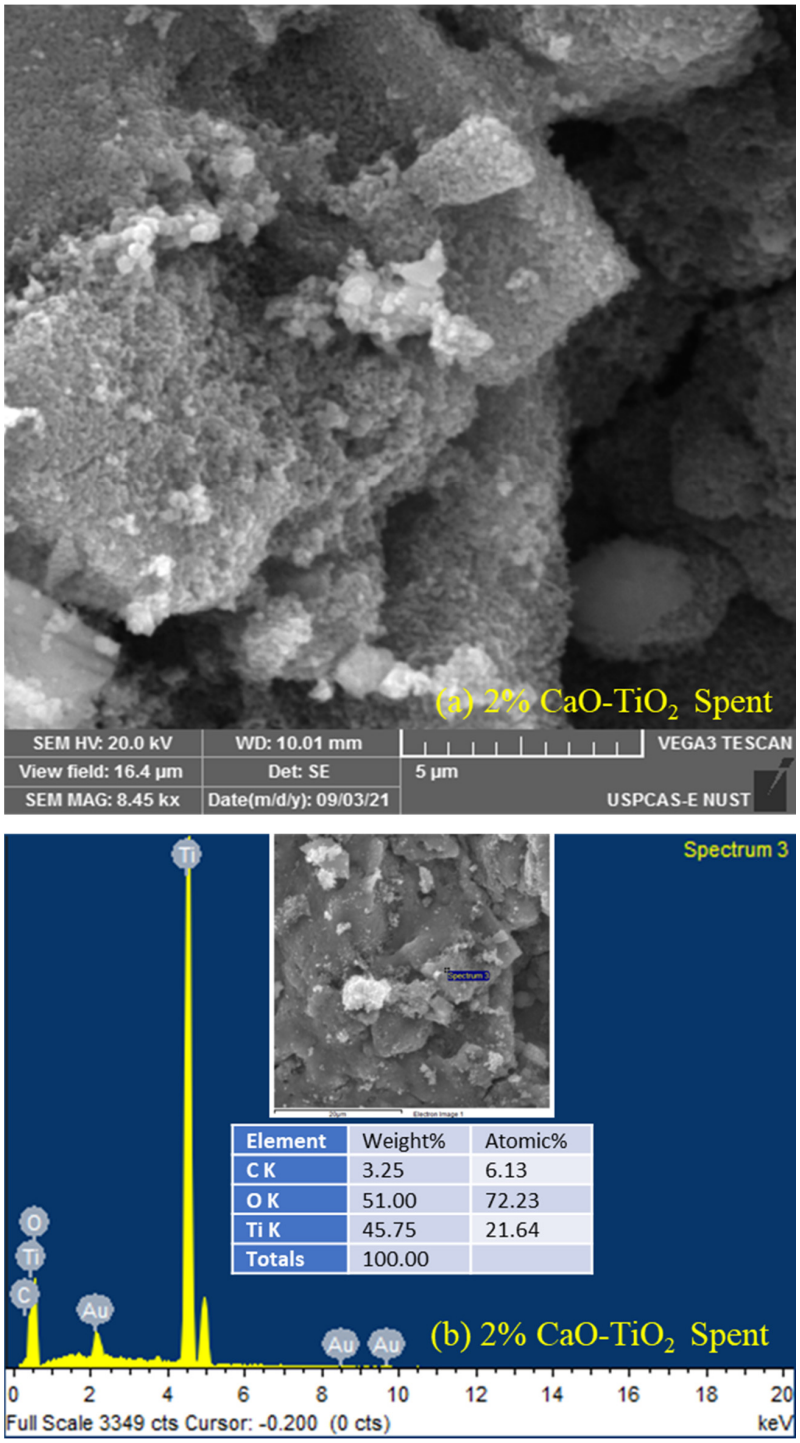

Figure 9. CaO loaded TiO_2 spent analysis (**a**) SEM (**b**) EDS analysis.

2.4. Reaction Mechanism

Catalytic partial oxidation is a complex reaction and its mechanism for H_2 and CO formation has not been clearly elucidated yet, but there is a possibility of two different mechanisms known as direct partial oxidation (DPO) and indirect combustion and reforming reaction [87]. Catalyst component, reaction conditions, metal-support interaction and various other factors affect the reaction mechanisms [88].

In direct partial oxidation, CH_4 dissociation followed by the formation of methyl radicals, H* and C* species (CH_3*, CH_2*, CH*, H*, C*) and oxidation of adsorbed molecular oxygen is subsequently converted into syngas. Thus, syngas is the primary product in direct partial oxidation Equation (1) [89]. While in indirect combustion and reforming reaction mechanism, CO_2 and H_2O formed as primary products, which may undergo steam or dry reforming and finally be converted into syngas Equation (2) [90].

$$CH_4 + 1/2O_2 \rightarrow CO + 2H_2 \tag{1}$$

$$CH_4 + 1/2O_2 \rightarrow CO_2 + H_2O \xrightarrow[CH_{4(unreacted)}]{} CO + H_2 \tag{2}$$

In POM heterogeneous catalysis, a solid base catalyst is generally characterized by the exposure of basic groups on the surface of the catalyst. Generally, basicity is illustrated by different metal oxides, such as CaO, TiO_2, MgO, ZrO_2, etc. [86]. Therefore, both oxides act as bases in CaO-TiO_2. Catalysts were activated for two hours before sampling in the presence of H_2 where CaO and TiO_2 donate their electron pairs through an interplay in a reduced atmosphere. Both metal oxides uncover O atoms, which may exist in different forms mainly O^{2-} surface adsorbed (SA) and O^{2-} surface lattice adsorbed (SLA) oxygen atoms [91] along with the formation of Ca^{2+} and Ti^{2+} ions Equations (3) and (4)). These positive ions or active sites are responsible for CH_4 adsorption and H_2 formation via different routes expressed in Figure 10. Uncovered O atoms are responsible for H^+ abstraction from the molecule of high acidity (CH_4) [86] and as a result, OH^- ions are formed which are further converted into water and lattice oxygen (O^{2-}) via OH^- coupling Equation (5). It is also noticeably significant that the conversion of CaO into its ions Equation (1), in which Ca^{2+} acts as Lewis acid (electrophile) and O^{2-} acts as Bronsted base. According to the definition of Lewis acid, it can accept the pair of non-bonding electrons, thus CaO reacts with a lone pair of H_2O (formed as a result of OH^- coupling) Equation (5) and converts into H_2 and $Ca(OH)_2$ Equation (6) that is quickly changed back into oxide again as a result of its thermal instability at high temperatures [39]. Lizuka et al. [92] explained the electrophilicity of Ca^{2+} cation, which is a weak acid due to its electronegativity and based on that, its conjugated base (O^{2-}) shows strong basicity. Thus, it can be concluded on the basis of the above discussion that more active sites along with added lattice oxygen will be available on support material that increases the basic nature of heterogeneous catalyst for enhancing catalytic performance. Furthermore, Equation (7) represents the interaction of Ti and Ca, resulting in the formation of H_2 molecules. Syngas can also be synthesized directly by the combination of adsorbed C and H_2O Equation (8). As a result of the increased oxygen consumption, more active sites are exposed to CH_4 adsorption and increased H_2 generation via different routes. [82,83] (Figure 10).

$$CaO \rightarrow Ca^{2+} + O^{2-} \xrightarrow[H_2]{} Ca_{(metallic)} \tag{3}$$

$$TiO_2 \rightarrow Ti^{2+} + O^{2-} \xrightarrow[H_2]{} Ti_{(metallic)} \tag{4}$$

$$OH^- + OH^- \rightarrow H_2O + O^{2-} \tag{5}$$

$$Ca^{2+} + 2H_2O \rightarrow Ca(OH)_2 + H_2 \tag{6}$$

$$TiO_2 + 2CaH_2 \rightarrow Ti^{2+} + 2CaO + 2H_2 \tag{7}$$

$$C + H_2O \rightarrow CO + H_2 \tag{8}$$

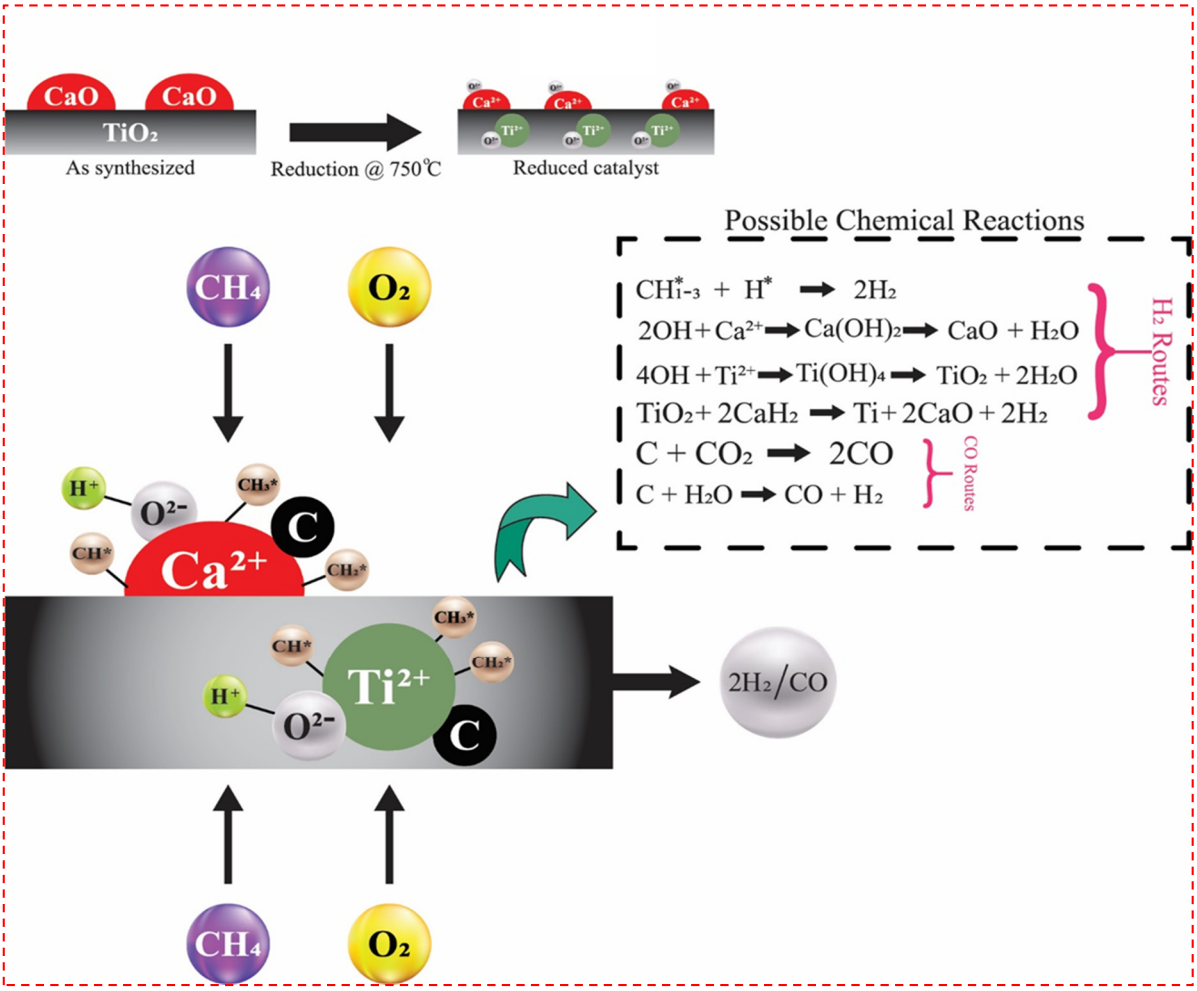

Figure 10. Partial oxidation of CH_4 to syngas over CaO-TiO_2 catalyst via different routes.

In combination with the literature and the above-mentioned analysis, it was observed that more active sites and uncover O atoms were generated with the involvement of both CaO and TiO_2 and these results propose direct POM over CaO-TiO_2 [82]. CO may oxidize further into CO_2 according to the following paths: Equations (9) and (10) [93]. However, it can be easily dissociated again into CO Equation (11) due to the involvement of anatase phase of TiO_2 as analyzed in XRD. It has also been explained in the literature that a low energy barrier is required for CO_2 dissociation into CO on anatase phase rather than that on a rutile phase of TiO_2 [82].

$$CO + OH \rightarrow CO_2 + H^+ \tag{9}$$

$$CO + O^{2-} \rightarrow CO_2 \tag{10}$$

$$C + CO_2 \rightarrow 2CO \tag{11}$$

3. Materials and Methods

3.1. Synthesis of CaO Doped TiO_2

A schematic illustration of waste derived CaO loaded TiO_2 nanostructures is depicted in (Figure 11). Titanium (IV) Tetra isopropoxide (TTIP) was used as a precursor to prepare TiO_2 sol by the sol-gel method. Analytical grade hydrochloric acid (HCl) was used for peptization and deionized (DI) water was utilized as dispersing media in TiO_2 synthesis [94]. All the chemicals were bought from Sigma Aldrich, St. Louis, Missouri, USA. Initially, the water-acid mixture was prepared and stabilized at 60 °C based on optimized methodology

as reported in the literature [95]. This temperature was kept constant throughout the experiment with continuous stirring and 5 mL TTIP was added into the reaction mixture dropwise for one minute and the resulting solution was continuously stirred at 1500 rpm for 1 h. As a result, a white thick precipitate was prepared that was gradually peptized after 2 h and a clear sol was obtained [96].

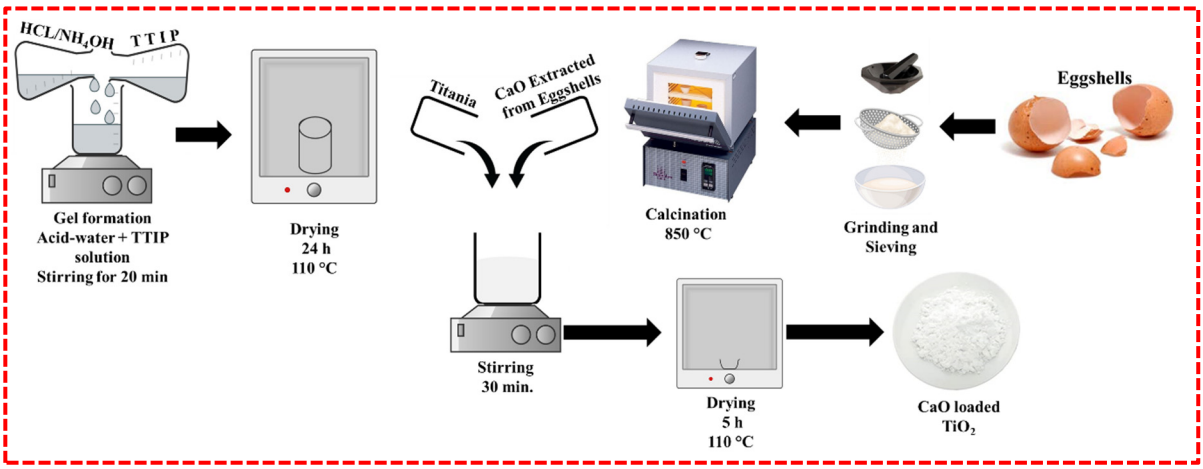

Figure 11. Schematic representation of synthesis of CaO decorated TiO_2 nanocomposites.

At neutral pH, TiO_2 sol is chemically unstable and can undergo agglomeration when it converts into gel form. Therefore, a solution of 30–50% concentrated HCl or NH_4OH was added dropwise into the reaction mixture to keep the pH acidic (3–7) and control the instability of the catalyst. Sol was converted into gel after vigorous stirring and a white suspension was prepared with high viscosity. The resulting mixture was allowed to dry at 110 °C in the oven for 24 h and a pale-yellow powder was obtained that was further washed with an organic solvent (ethanol) and water subsequently to remove impurities, and was again dried at the same temperature to get the final product [97].

CaO was obtained from eggshells by simply grinding followed by sieving with 1 µm sieve. Finally, waste derived 1%, 2% and 3% by weight CaO loading on TiO_2 was carried out by employing a wetness impregnation method. Briefly, 1 g TiO_2 was added in water and kept on stirring for 30 min, a specified percentage of CaO was then added under continuous stirring at 1500 rpm and again continuously stirred for 5 h. A final homogenous solution was placed overnight in the oven and a final product was calcined at 850 °C for 5 h to remove the traces of impurities.

3.2. Material Characterisation

D8 Advance (Bruker Advanced, Germany) equipped with CuKα radiations of wavelength 1.5406 Å at 40 kV was used for the structural analysis of synthesized catalysts [98]. Ni filter was used for filtering background radiations. XRD scans were obtained in the range of 2θ = 10–90° with a scan rate of 2°/min. Furthermore, the crystallographic properties were ascertained by utilizing MDI JADE 6.5 software. Further crystallite size of samples was obtained with the help of the Scherrer equation (Equation (12)).

$$D_p = \frac{0.94\lambda}{\beta Cos\theta} \tag{12}$$

where D_p is the crystallite size, β is line broadening in radian, θ is Bragg angle and λ is X-ray wavelength.

Raman spectroscopy was performed by using BWS415-532S, USA for structural identification and carbon deposited on the surface of the catalyst during the time on stream. FTIR was carried out using a model Cary 630 (Agilent Technologies, Santa Clara, CA, USA) to investigate the chemical analysis and functional groups. Spectra were recorded in the

range of 4000 to 650 cm^{-1}. TGA-DTG was used for the evaluation of thermal stability and weight loss in both fresh catalysts and spent. Experiments were carried out in TGA 500 (TA Instruments, New Castle, DE, USA) where the catalyst was purged by the N_2 flow rate of 35 mL/min for 30 min. The morphological properties and elemental analysis of fresh and spent catalyst were observed by SEM-EDX using the JEOL JSM- 6490A (JEOL Ltd., Tokyo, Japan) having 200 nm resolution.

3.3. Partial Oxidation of Methane Setup

A fixed bed thermal reactor (Parr instruments 5401, St, Moline, IL, USA) was used for methane cracking as shown in Figure 12. The experimental setup consists of three main parts including a gas feed system (GFS), vertical stainless steel fixed bed reactor (SS 316) having a length of 300 mm with an inner diameter of 12 nm, and an analysis system for product gases. Initially, the catalyst was placed in the middle of the thermal reactor and reactant gases (CH_4 (99.99%) and O_2) were allowed to pass through and mass flow controllers (Brooke instruments, Hatfield, PA, USA) were used to control the flow of the reactant gasses. Process controller (4871, Parr instruments) integrated with thermocouples and pressure gauge (2.5 bar) was used to control the temperature and pressure of the reactor, respectively. An online SCADA system was employed to monitor the flow rate and temperature as POM reaction was carried out at 750 °C with a total flow rate of 30 mL/min. Finally, CH_4 and the product gases were analyzed by gas chromatography (GC-TCD) (GC-2010 Plus, Shimadzu, Kyoto, Japan) equipped with a thermal conductivity detector (TCD) (RT-MS5A, 30 m × 0.32 mm, ID 30 µm) for the detection of different gases [37].

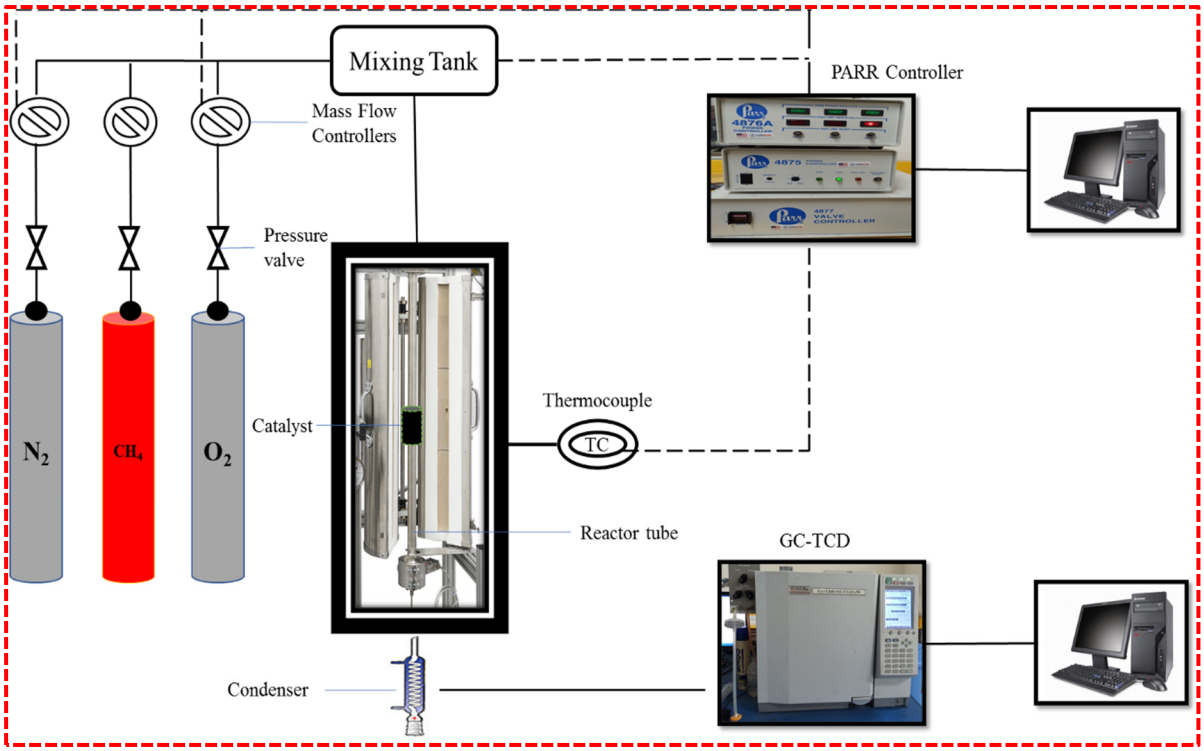

Figure 12. Experimental setup for POM reaction in a fixed bed reactor.

3.4. Calculations

The performance of catalyst for POM was analyzed based on CH_4 conversion (Equation (13)), H_2 selectivity (Equation (14)) and CO selectivity (Equation (15)) and H_2/CO ratio (Equation (16)).

$$CH_4 \text{ conversion } (X_{CH_4})\% = \left[\frac{(n\,CH_4)_{converted}}{(n\,CH_4)_{feed}} \times 100\right] \tag{13}$$

$$H_2 \text{ selectivity } (S_{H_2})\% = \left[\frac{(nH_2)_{produced}}{(2 \times nCH_4)_{converted}} \times 100\right] \tag{14}$$

$$CO \text{ selectivity } (S_{CO})\% = \left[\frac{(nCO)_{produced}}{(nCH_4)_{converted}} \times 100\right] \tag{15}$$

$$H_2/CO \text{ ratio } = \left[\frac{\text{selectivity}(S_{H_2})}{\text{selectivity}(S_{CO})}\right] \tag{16}$$

4. Conclusions

TiO_2 anatase phase free from impurities and other phases such as rutile were successfully synthesized by employing the sol-gel method. Pristine TiO_2 and CaO decorated on the surface of TiO_2 by wetness impregnation method were confirmed by utilizing structural, elemental, and morphological techniques. The findings revealed that the TiO_2 nanostructures influenced the surface metal oxide deposition resulting in the fully exposed active phases. Among the catalyst, both 2% and 3% CaO loaded TiO_2 have shown higher conversion efficiency in comparison to pure and 1% CaO loaded TiO_2. No distinct change in conversion efficiencies for 2% and 3% were observed confirming that an optimal loading is achieved. Finally, 2% and 3% CaO loaded TiO_2 have shown the average conversion efficiency of 83.56 and 79.54 and H_2/CO ratio 2.25 and 2.28, respectively. These catalysts prepared during this study have the advantage of a low cost and simple preparation method of TiO_2, even at low temperatures along with high catalytic activity for syngas production via the POM route.

Author Contributions: Conceptualization, A.H.K.; data curation, A.H.J., N.N. and S.S.; formal analysis, A.H.J. and U.Y.Q.; investigation, A.H.K., S.S. and Z.A.; methodology, A.H.K., N.N. and Z.A.; project administration, S.R.N.; resources, S.R.N.; software, Z.A.; supervision, U.R.; validation, I.U.D.; visualization, I.U.D. and U.Y.Q.; writing—original draft, A.H.K., A.H.J. and S.S.; writing—review and editing, S.R.N., I.U.D., U.R. and U.Y.Q. All authors have read and agreed to the published version of the manuscript.

Funding: This research received no external funding.

Data Availability Statement: Not applicable.

Conflicts of Interest: The authors declare no conflict of interest.

References

1. Arandiyan, H.; Li, J.; Ma, L.; Hashemnejad, S.; Mirzaei, M.; Chen, J.; Chang, H.; Liu, C.; Wang, C.; Chen, L. Methane reforming to syngas over LaNixFe1−xO$_3$ ($0 \leq x \leq 1$) mixed-oxide perovskites in the presence of CO_2 and O_2. *J. Ind. Eng. Chem.* **2012**, *18*, 2103–2114. [CrossRef]
2. Wei, Q.; Yang, G.; Gao, X.; Yamane, N.; Zhang, P.; Liu, G.; Tsubaki, N. Ni/Silicalite-1 coating being coated on SiC foam: A tailor-made monolith catalyst for syngas production using a combined methane reforming process. *Chem. Eng. J.* **2017**, *327*, 465–473. [CrossRef]
3. Olah, G.A.; Goeppert, A.; Czaun, M.; Mathew, T.; May, R.B.; Prakash, G.S. Single step bi-reforming and oxidative bi-reforming of methane (natural gas) with steam and carbon dioxide to metgas (CO-2H_2) for methanol synthesis: Self-sufficient effective and exclusive oxygenation of methane to methanol with oxygen. *J. Am. Chem. Soc.* **2015**, *137*, 8720–8729. [CrossRef] [PubMed]
4. Wei, Q.; Gao, X.; Liu, G.; Yang, R.; Zhang, H.; Yang, G.; Yoneyama, Y.; Tsubaki, N. Facile one-step synthesis of mesoporous Ni-Mg-Al catalyst for syngas production using coupled methane reforming process. *Fuel* **2018**, *211*, 1–10. [CrossRef]

5. Xing, C.; Yang, G.; Wu, M.; Yang, R.; Tan, L.; Zhu, P.; Wei, Q.; Li, J.; Mao, J.; Yoneyama, Y. Hierarchical zeolite Y supported cobalt bifunctional catalyst for facilely tuning the product distribution of Fischer–Tropsch synthesis. *Fuel* **2015**, *148*, 48–57. [CrossRef]
6. Ding, H.; Xu, Y.; Luo, C.; Wang, Q.; Shen, C.; Xu, J.; Zhang, L. A novel composite perovskite-based material for chemical-looping steam methane reforming to hydrogen and syngas. *Energy Convers. Manag.* **2018**, *171*, 12–19. [CrossRef]
7. Horn, R.; Schlögl, R. Methane activation by heterogeneous catalysis. *Catal. Lett.* **2015**, *145*, 23–39. [CrossRef]
8. Choudhary, V.R.; Mondal, K.C. CO_2 reforming of methane combined with steam reforming or partial oxidation of methane to syngas over NdCoO3 perovskite-type mixed metal-oxide catalyst. *Appl. Energy* **2006**, *83*, 1024–1032. [CrossRef]
9. Cao, D.; Ding, H.; Luo, C.; Wu, F.; Li, X.; Zhang, L. Development of a cordierite monolith reactor coated with CeO_2-supported BaSrCo-based perovskite for chemical looping steam methane reforming. *Fuel Processing Technol.* **2021**, *220*, 106889. [CrossRef]
10. Nematollahi, B.; Rezaei, M.; Khajenoori, M. Combined dry reforming and partial oxidation of methane to synthesis gas on noble metal catalysts. *Int. J. Hydrogen Energy* **2011**, *36*, 2969–2978. [CrossRef]
11. Nguyen, T.T.; Yamaki, T.; Taniguchi, S.; Endo, A.; Kataoka, S. Integrating life cycle assessment for design and optimization of methanol production from combining methane dry reforming and partial oxidation. *J. Clean. Prod.* **2021**, *292*, 125970. [CrossRef]
12. Khoja, A.H.; Tahir, M.; Saidina Amin, N.A. Evaluating the Performance of a Ni Catalyst Supported on La_2O_3-$MgAl_2O_4$ for Dry Reforming of Methane in a Packed Bed Dielectric Barrier Discharge Plasma Reactor. *Energy Fuels* **2019**, *33*, 11630–11647. [CrossRef]
13. Costa, D.S.; Gomes, R.S.; Rodella, C.B.; da Silva Junior, R.B.; Frety, R.; Neto, É.T.; Brandão, S.T. Study of nickel, lanthanum and niobium-based catalysts applied in the partial oxidation of methane. *Catal. Today* **2020**, *344*, 15–23. [CrossRef]
14. Elbadawi, A.H.; Ge, L.; Li, Z.; Liu, S.; Wang, S.; Zhu, Z. Catalytic partial oxidation of methane to syngas: Review of perovskite catalysts and membrane reactors. *Catal. Rev.* **2021**, *63*, 1–67. [CrossRef]
15. Zhang, Y.-K.; Zhao, Y.-J.; Yi, Q.; Wei, G.-Q.; Shi, L.-J.; Zhou, H. NiO/κ-$CeZrO_4$ functional oxygen carriers with Niδ+ and oxygen vacancy synergy for chemical looping partial oxidation reforming of methane. *Fuel Process. Technol.* **2021**, *219*, 106875. [CrossRef]
16. Kim, H.W.; Kang, K.M.; Kwak, H.-Y. Preparation of supported Ni catalysts with a core/shell structure and their catalytic tests of partial oxidation of methane. *Int. J. Hydrogen Energy* **2009**, *34*, 3351–3359. [CrossRef]
17. Ma, Q.; Guo, L.; Fang, Y.; Li, H.; Zhang, J.; Zhao, T.-S.; Yang, G.; Yoneyama, Y.; Tsubaki, N. Combined methane dry reforming and methane partial oxidization for syngas production over high dispersion Ni based mesoporous catalyst. *Fuel Process. Technol.* **2019**, *188*, 98–104. [CrossRef]
18. Rostrupnielsen, J.; Hansen, J.B. CO_2-reforming of methane over transition metals. *J. Catal.* **1993**, *144*, 38–49. [CrossRef]
19. Jin, R.; Chen, Y.; Li, W.; Cui, W.; Ji, Y.; Yu, C.; Jiang, Y. Mechanism for catalytic partial oxidation of methane to syngas over a Ni/Al_2O_3 catalyst. *Appl. Catal. A Gen.* **2000**, *201*, 71–80. [CrossRef]
20. Pompeo, F.; Nichio, N.N.; Ferretti, O.A.; Resasco, D. Study of Ni catalysts on different supports to obtain synthesis gas. *Int. J. Hydrogen Energy* **2005**, *30*, 1399–1405. [CrossRef]
21. Guo, S.; Wang, J.; Ding, C.; Duan, Q.; Ma, Q.; Zhang, K.; Liu, P. Confining Ni nanoparticles in honeycomb-like silica for coking and sintering resistant partial oxidation of methane. *Int. J. Hydrogen Energy* **2018**, *43*, 6603–6613. [CrossRef]
22. Védrine, J.C. Heterogeneous catalysis on metal oxides. *Catalysts* **2017**, *7*, 341. [CrossRef]
23. Hattori, H. Solid base catalysts: Fundamentals and their applications in organic reactions. *Appl. Catal. A Gen.* **2015**, *504*, 103–109. [CrossRef]
24. Kwong, T.-L.; Yung, K.-F. Heterogeneous alkaline earth metal–transition metal bimetallic catalysts for synthesis of biodiesel from low grade unrefined feedstock. *RSC Adv.* **2015**, *5*, 83748–83756. [CrossRef]
25. Fleys, M.; Simon, Y.; Swierczynski, D.; Kiennemann, A.; Marquaire, P.-M. Investigation of the Reaction of Partial Oxidation of Methane over Ni/La_2O_3 Catalyst. *Energy Fuels* **2006**, *20*, 2321–2329. [CrossRef]
26. Choudhary, V.; Rajput, A.; Rane, V. Low temperature oxidative conversion of methane to synthesis gas over Co/rare earth oxide catalysts. *Catal. Lett.* **1992**, *16*, 269–272. [CrossRef]
27. Christian Enger, B.; Lødeng, R.; Holmen, A. A review of catalytic partial oxidation of methane to synthesis gas with emphasis on reaction mechanisms over transition metal catalysts. *Appl. Catal. A Gen.* **2008**, *346*, 1–27. [CrossRef]
28. Dedov, A.; Loktev, A.; Danilov, V.; Krasnobaeva, O.; Nosova, T.; Mukhin, I.; Baranchikov, A.; Yorov, K.E.; Bykov, M.; Moiseev, I. Catalytic Materials Based on Hydrotalcite-Like Aluminum, Magnesium, Nickel, and Cobalt Hydroxides: Effect of the Nickel/Cobalt Ratio on the Results of Partial Oxidation and Dry Reforming of Methane to Synthesis Gas. *Pet. Chem.* **2020**, *60*, 194–203. [CrossRef]
29. Zhang, S.-Y.; Ma, J.-J.; Zhu, H.-L.; Zheng, Y.-Q. Self-supported beaded Au@ Co_3O_4 nanowire arrays perform electrocatalytic CO_2 reduction in water to syngas and water oxidation to O_2. *New J. Chem.* **2020**, *44*, 11808–11816. [CrossRef]
30. Jalali, R.; Rezaei, M.; Nematollahi, B.; Baghalha, M. Preparation of Ni/$MeAl_2O_4$-$MgAl_2O_4$ (Me = Fe, Co, Ni, Cu, Zn, Mg) nanocatalysts for the syngas production via combined dry reforming and partial oxidation of methane. *Renew. Energy* **2020**, *149*, 1053–1067. [CrossRef]
31. Martínez-Navarro, B.; Sanchis, R.; Asedegbega-Nieto, E.; Solsona, B.; Ivars-Barceló, F. (Ag) Pd-Fe_3O_4 Nanocomposites as Novel Catalysts for Methane Partial Oxidation at Low Temperature. *Nanomaterials* **2020**, *10*, 988. [CrossRef] [PubMed]
32. Simonov, M.; Bespalko, Y.; Smal, E.; Valeev, K.; Fedorova, V.; Krieger, T.; Sadykov, V. Nickel-Containing Ceria-Zirconia Doped with Ti and Nb. Effect of Support Composition and Preparation Method on Catalytic Activity in Methane Dry Reforming. *Nanomaterials* **2020**, *10*, 1281. [CrossRef]

33. Barona, M.; Gaggioli, C.A.; Gagliardi, L.; Snurr, R.Q. DFT Study on the Catalytic Activity of ALD-Grown Diiron Oxide Nanoclusters for Partial Oxidation of Methane to Methanol. *J. Phys. Chem. A* **2020**, *124*, 1580–1592. [CrossRef]
34. Khaleel, A.; Jobe, S.; Ahmed, M.a.; Al-Zuhair, S.; Tariq, S. Enhanced selectivity of syngas in partial oxidation of methane: A new route for promising Ni-alumina catalysts derived from Ni/γ-AlOOH with modified Ni dispersion. *Int. J. Energy Res.* **2020**, *44*, 12081–12099. [CrossRef]
35. Świrk, K.; Grams, J.; Motak, M.; Da Costa, P.; Grzybek, T. Understanding of tri-reforming of methane over Ni/Mg/Al hydrotalcite-derived catalyst for CO_2 utilization from flue gases from natural gas-fired power plants. *J. CO_2 Util.* **2020**, *42*, 101317. [CrossRef]
36. Munawar, M.A.; Khoja, A.H.; Hassan, M.; Liaquat, R.; Naqvi, S.R.; Mehran, M.T.; Abdullah, A.; Saleem, F. Biomass ash characterization, fusion analysis and its application in catalytic decomposition of methane. *Fuel* **2021**, *285*, 119107. [CrossRef]
37. Raza, J.; Khoja, A.H.; Naqvi, S.R.; Mehran, M.T.; Shakir, S.; Liaquat, R.; Tahir, M.; Ali, G. Methane decomposition for hydrogen production over biomass fly ash-based CeO_2 nanowires promoted cobalt catalyst. *J. Environ. Chem. Eng.* **2021**, *9*, 105816. [CrossRef]
38. Calero, J.; Luna, D.; Sancho, E.D.; Luna, C.; Bautista, F.M.; Romero, A.A.; Posadillo, A.; Verdugo, C. Development of a new biodiesel that integrates glycerol, by using CaO as heterogeneous catalyst, in the partial methanolysis of sunflower oil. *Fuel* **2014**, *122*, 94–102. [CrossRef]
39. Tavizón-Pozos, J.A.; Chavez-Esquivel, G.; Suárez-Toriello, V.A.; Santolalla-Vargas, C.E.; Luévano-Rivas, O.A.; Valdés-Martínez, O.U.; Talavera-López, A.; Rodriguez, J.A. State of Art of Alkaline Earth Metal Oxides Catalysts Used in the Transesterification of Oils for Biodiesel Production. *Energies* **2021**, *14*, 1031. [CrossRef]
40. Corma, A.; Iborra, S. Optimization of Alkaline Earth Metal Oxide and Hydroxide Catalysts for Base-Catalyzed Reactions. In *Advances in Catalysis*; Gates, B.C., Knözinger, H., Eds.; Academic Press: Cambridge, MA, USA, 2006; Volume 49, pp. 239–302.
41. Javed, A.H.; Shahzad, N.; Butt, F.A.; Khan, M.A.; Naeem, N.; Liaquat, R.; Khoja, A.H. Synthesis of bimetallic Co-Ni/ZnO nanoprisms (ZnO-NPr) for hydrogen-rich syngas production via partial oxidation of methane. *J. Environ. Chem. Eng.* **2021**, *9*, 106887. [CrossRef]
42. Qiu, Y.; Chen, J.; Zhang, J. Effects of CeO_2 and CaO composite promoters on the properties of eggshell Ni/MgO-Al_2O_3 catalysts for partial oxidation of methane to syngas. *React. Kinet. Catal. Lett.* **2008**, *94*, 351–357. [CrossRef]
43. Mateos-Pedrero, C.; González-Carrazán, S.R.; Soria, M.A.; Ruíz, P. Effect of the nature of TiO2 support over the performances of Rh/TiO2 catalysts in the partial oxidation of methane. *Catal. Today* **2013**, *203*, 158–162. [CrossRef]
44. Baamran, K.S.; Tahir, M.; Mohamed, M.; Hussain Khoja, A. Effect of support size for stimulating hydrogen production in phenol steam reforming using Ni-embedded TiO_2 nanocatalyst. *J. Environ. Chem. Eng.* **2020**, *8*, 103604. [CrossRef]
45. Yan, Q.; Weng, W.Z.; Wan, H.L.; Toghiani, H.; Toghiani, R.K.; Pittman, C. Activation of methane to syngas over a Ni/TiO_2 catalyst. *Appl. Catal. A Gen.* **2003**, *239*, 43–58. [CrossRef]
46. Perkas, N.; Zhong, Z.; Chen, L.; Besson, M.; Gedanken, A. Sonochemically prepared high dispersed Ru/TiO_2 mesoporous catalyst for partial oxidation of methane to syngas. *Catal. Lett.* **2005**, *103*, 9–14. [CrossRef]
47. Elmasides, C.; Kondarides, D.I.; Neophytides, S.G.; Verykios, X.E. Partial Oxidation of Methane to Synthesis Gas over Ru/TiO_2 Catalysts: Effects of Modification of the Support on Oxidation State and Catalytic Performance. *J. Catal.* **2001**, *198*, 195–207. [CrossRef]
48. Efstathiou, A.M.; Kladi, A.; Tsipouriari, V.A.; Verykios, X.E. Reforming of Methane with Carbon Dioxide to Synthesis Gas over Supported Rhodium Catalysts: II. A Steady-State Tracing Analysis: Mechanistic Aspects of the Carbon and Oxygen Reaction Pathways to Form CO. *J. Catal.* **1996**, *158*, 64–75. [CrossRef]
49. Wu, T.; Yan, Q.; Wan, H. Partial oxidation of methane to hydrogen and carbon monoxide over a Ni/TiO_2 catalyst. *J. Mol. Catal. A Chem.* **2005**, *226*, 41–48. [CrossRef]
50. Bradford, M.C.; Vannice, M. Metal-support interactions during the CO_2 reforming of CH_4 over model TiOx/Pt catalysts. *Catal. Lett.* **1997**, *48*, 31–38. [CrossRef]
51. Znaidi, L.; Seraphimova, R.; Bocquet, J.; Colbeau-Justin, C.; Pommier, C. A semi-continuous process for the synthesis of nanosize TiO_2 powders and their use as photocatalysts. *Mater. Res. Bull.* **2001**, *36*, 811–825. [CrossRef]
52. Wu, Z.; Tang, N.; Xiao, L.; Liu, Y.; Wang, H. MnOx/TiO_2 composite nanoxides synthesized by deposition-precipitation method as a superior catalyst for NO oxidation. *J. Colloid Interface Sci.* **2010**, *352*, 143–148. [CrossRef] [PubMed]
53. Bazli, L.; Siavashi, M.; Shiravi, A. A review of carbon nanotube/TiO_2 composite prepared via sol-gel method. *J. Compos. Compd.* **2019**, *1*, 1–9. [CrossRef]
54. Vijayalakshmi, R.; Rajendran, V. Synthesis and characterization of nano-TiO_2 via different methods. *Arch. Appl. Sci. Res.* **2012**, *4*, 1183–1190.
55. You, Y.F.; Xu, C.H.; Xu, S.S.; Cao, S.; Wang, J.P.; Huang, Y.B.; Shi, S.Q. Structural characterization and optical property of TiO_2 powders prepared by the sol–gel method. *Ceram. Int.* **2014**, *40*, 8659–8666. [CrossRef]
56. Lai, C.W. Modification of one-dimensional TiO_2 nanotubes with CaO dopants for high CO_2 adsorption. *Int. J. Photoenergy* **2014**, *2014*, 471713. [CrossRef]
57. Gu, L.; Wang, J.; Cheng, H.; Du, Y.; Han, X. Synthesis of nano-sized anatase TiO_2 with reactive {001} facets using lamellar protonated titanate as precursor. *Chem. Commun.* **2012**, *48*, 6978–6980. [CrossRef]

58. Da Cunha, T.; Maulu, A.; Guillot, J.; Fleming, Y.; Duez, B.; Lenoble, D.; Arl, D. Design of Silica Nanoparticles-Supported Metal Catalyst by Wet Impregnation with Catalytic Performance for Tuning Carbon Nanotubes Growth. *Catalysts* **2021**, *11*, 986. [CrossRef]
59. Shakir, S.; Khan, Z.S.; Ali, A.; Akbar, N.; Musthaq, W. Development of copper doped titania based photoanode and its performance for dye sensitized solar cell applications. *J. Alloys Compd.* **2015**, *652*, 331–340. [CrossRef]
60. Challagulla, S.; Tarafder, K.; Ganesan, R.; Roy, S. Structure sensitive photocatalytic reduction of nitroarenes over TiO_2. *Sci. Rep.* **2017**, *7*, 1–11. [CrossRef]
61. Ponomarev, V.A.; Orlov, E.A.; Malikov, N.A.; Tarasov, Y.V.; Sheveyko, A.N.; Permyakova, E.S.; Kuptsov, K.A.; Dyatlov, I.A.; Ignatov, S.G.; Ilnitskaya, A.S.; et al. Ag(Pt) nanoparticles-decorated bioactive yet antibacterial Ca- and P-doped TiO_2 coatings produced by plasma electrolytic oxidation and ion implantation. *Appl. Surf. Sci.* **2020**, *516*, 146068. [CrossRef]
62. Rattana, T. The Structural, morphological and optical properties of Ca doped TiO2 thin films prepared by sol-gel method. *SNRU J. Sci. Technol.* **2018**, *10*, 1–5.
63. Castro, Y.; Durán, A. Ca doping of mesoporous TiO_2 films for enhanced photocatalytic efficiency under solar irradiation. *J. Sol-Gel Sci. Technol.* **2016**, *78*, 482–491. [CrossRef]
64. Liu, Z.; Jian, Z.; Fang, J.; Xu, X.; Zhu, X.; Wu, S. Low-Temperature Reverse Microemulsion Synthesis, Characterization, and Photocatalytic Performance of Nanocrystalline Titanium Dioxide. *Int. J. Photoenergy* **2012**, *2012*, 702503. [CrossRef]
65. Ramasamy, V.; Mohana, V.; Rajendran, V. Characterization of Ca doped CeO_2 quantum dots and their applications in photocatalytic degradation. *OpenNano* **2018**, *3*, 38–47. [CrossRef]
66. Kalaivani, T.; Anilkumar, P. Role of temperature on the phase modification of TiO_2 nanoparticles synthesized by the precipitation method. *Silicon* **2018**, *10*, 1679–1686. [CrossRef]
67. Rosa, S.; Nossol, A.; Nossol, E.; Zarbin, A.; Peralta-Zamora, P. Non-Synergistic UV-A Photocatalytic Degradation of Estrogens by Nano-TiO 2 Supported on Activated Carbon. *J. Braz. Chem. Soc.* **2017**, *28*, 582. [CrossRef]
68. Ramimoghadam, D.; Bagheri, S.; Abd Hamid, S.B. Biotemplated Synthesis of Anatase Titanium Dioxide Nanoparticles via Lignocellulosic Waste Material. *BioMed Res. Int.* **2014**, *2014*, 205636. [CrossRef] [PubMed]
69. Siang, T.J.; Jalil, A.A.; Liew, S.Y.; Owgi, A.H.K.; Rahman, A.F.A. A review on state-of-the-art catalysts for methane partial oxidation to syngas production. *Catal. Rev.* **2022**, 1–57. [CrossRef]
70. Pulišová, P.; Boháček, J.; Šubrt, J.; Szatmáry, L.; Bezdička, P.; Večerníková, E.; Balek, V. Thermal behaviour of titanium dioxide nanoparticles prepared by precipitation from aqueous solutions. *J. Therm. Anal. Calorim.* **2010**, *101*, 607–613. [CrossRef]
71. Hernández, J.V. Structural and Morphological Modification of TiO2 Doped Metal Ions and Investigation of Photo-Induced Charge Transfer Processes. 2017. Available online: https://tel.archives-ouvertes.fr/tel-01954392/document (accessed on 5 February 2022).
72. Sridevi, D.V.; Vadivel, R.; Thirupathi, S.; Geetha, K.; Prabu, R.; Karthikeyan, J.; Rajarajan, K.; Ramachadran, K. Synthesis, Structural and Optical Properties of Co Doped TiO_2 Nanocrystals by Sol-Gel Method. *Mech. Mater. Sci. Eng. J.* **2017**, *9*. Available online: https://mmse.xyz/en/synthesis-structural-and-optical-properties-of-co-doped-tio2-nanocrystals-by-sol-gel-method/ (accessed on 26 July 2022).
73. Al-Taweel, S.S.; Saud, H.R. New route for synthesis of pure anatase TiO_2 nanoparticles via utrasound-assisted sol-gel method. *J. Chem. Pharm. Res* **2016**, *8*, 620–626.
74. Biru, M.; Qaderi, J.; Mamat, C.R.; Jalil, A.A. Preparation and Characterization of Copper, Iron, and Nickel Doped Titanium Dioxide Photocatalysts for Decolorization of Methylene Blue. *Sains Malays.* **2021**, *50*, 135–149.
75. Lugo, V.R.; Mondragón-Galicia, G.; Gutiérrez-Martínez, A.; Gutiérrez-Wing, C.; González, O.R.; López, P.; Salinas-Hernández, P.; Tzompantzi, F.; Valderrama, M.I.R.; Pérez-Hernández, R. Pt–Ni/ZnO-rod catalysts for hydrogen production by steam reforming of methanol with oxygen. *RSC Adv.* **2020**, *10*, 41315–41323. [CrossRef]
76. Matras, D.; Jacques, S.D.; Poulston, S.; Grosjean, N.; Estruch Bosch, C.; Rollins, B.; Wright, J.; Di Michiel, M.; Vamvakeros, A.; Cernik, R.J. Operando and postreaction diffraction imaging of the La–Sr/CaO catalyst in the oxidative coupling of methane reaction. *J. Phys. Chem. C* **2019**, *123*, 1751–1760. [CrossRef]
77. Djinović, P.; Črnivec, I.G.O.; Erjavec, B.; Pintar, A. Influence of active metal loading and oxygen mobility on coke-free dry reforming of Ni–Co bimetallic catalysts. *Appl. Catal. B Environ.* **2012**, *125*, 259–270. [CrossRef]
78. Rui, Z.; Feng, D.; Chen, H.; Ji, H. Anodic TiO_2 nanotube array supported nickel–noble metal bimetallic catalysts for activation of CH_4 and CO_2 to syngas. *Int. J. Hydrogen Energy* **2014**, *39*, 16252–16261. [CrossRef]
79. Singh, G.; Kumar, S.; Sharma, S.K.; Sharma, M.; Singh, V.P.; Vaish, R. Antibacterial and photocatalytic active transparent TiO_2 crystallized CaO–BaO–B2O3–Al2O3–TiO2–ZnO glass nanocomposites. *J. Am. Ceram. Soc.* **2019**, *102*, 3378–3390. [CrossRef]
80. Kikuchi, E.; Chen, Y. Syngas formation by partial oxidation of methane in palladium membrane reactor. *Stud. Surf. Sci. Catal.* **1998**, *119*, 441–446. [CrossRef]
81. De Santana Santos, M.; Neto, R.C.R.; Noronha, F.B.; Bargiela, P.; da Rocha, M.d.G.C.; Resini, C.; Carbó-Argibay, E.; Fréty, R.; Brandão, S.T. Perovskite as catalyst precursors in the partial oxidation of methane: The effect of cobalt, nickel and pretreatment. *Catal. Today* **2018**, *299*, 229–241. [CrossRef]
82. Guo, D.; Wang, G.-C. Partial oxidation of methane on anatase and rutile defective TiO_2 supported Rh4 cluster: A density functional theory study. *J. Phys. Chem. C* **2017**, *121*, 26308–26320. [CrossRef]

83. Irfan, M.; Li, A.; Zhang, L.; Javid, M.; Wang, M.; Khushk, S. Enhanced H_2 Production from Municipal Solid Waste Gasification Using Ni–CaO–TiO_2 Bifunctional Catalyst Prepared by dc Arc Plasma Melting. *Ind. Eng. Chem. Res.* **2019**, *58*, 13408–13419. [CrossRef]
84. Luisetto, I.; Tuti, S.; Battocchio, C.; Mastro, S.L.; Sodo, A. Ni/CeO_2–Al_2O_3 catalysts for the dry reforming of methane: The effect of $CeAlO_3$ content and nickel crystallite size on catalytic activity and coke resistance. *Appl. Catal. A Gen.* **2015**, *500*, 12–22. [CrossRef]
85. Dychalska, A.; Popielarski, P.; Franków, W.; Fabisiak, K.; Paprocki, K.; Szybowicz, M. Study of CVD diamond layers with amorphous carbon admixture by Raman scattering spectroscopy. *Mater. Sci.* **2015**, *33*, 799–805. [CrossRef]
86. Nath, B.D.; Takaishi, K.; Ema, T. Macrocyclic multinuclear metal complexes acting as catalysts for organic synthesis. *Catal. Sci. Technol.* **2020**, *10*, 12–34. [CrossRef]
87. Ma, R.; Xu, B.; Zhang, X. Catalytic partial oxidation (CPOX) of natural gas and renewable hydrocarbons/oxygenated hydrocarbons—A review. *Catal. Today* **2019**, *338*, 18–30. [CrossRef]
88. Osman, A.I. Catalytic hydrogen production from methane partial oxidation: Mechanism and kinetic study. *Chem. Eng. Technol.* **2020**, *43*, 641–648. [CrossRef]
89. Liu, T.; Snyder, C.; Veser, G. Catalytic Partial Oxidation of Methane: Is a Distinction between Direct and Indirect Pathways Meaningful? *Ind. Eng. Chem. Res.* **2007**, *46*, 9045–9052. [CrossRef]
90. Heitnes, K.; Lindberg, S.; Rokstad, O.A.; Holmen, A. Catalytic partial oxidation of methane to synthesis gas. *Catal. Today* **1995**, *24*, 211–216. [CrossRef]
91. Qiu, Y.; Chen, J.; Zhang, J. Effect of CeO_2 and CaO promoters on ignition performance for partial oxidation of methane over Ni/MgO-Al_2O_3 catalyst. *J. Nat. Gas Chem.* **2007**, *16*, 148–154. [CrossRef]
92. Iizuka, T.; Hattori, H.; Ohno, Y.; Sohma, J.; Tanabe, K. Basic sites and reducing sites of calcium oxide and their catalytic activities. *J. Catal.* **1971**, *22*, 130–139. [CrossRef]
93. Maestri, M.; Vlachos, D.G.; Beretta, A.; Forzatti, P.; Groppi, G.; Tronconi, E. Dominant reaction pathways in the catalytic partial oxidation of CH 4 on Rh. *Top. Catal.* **2009**, *52*, 1983. [CrossRef]
94. Yazid, S.A.; Rosli, Z.M.; Juoi, J.M. Effect of titanium (IV) isopropoxide molarity on the crystallinity and photocatalytic activity of titanium dioxide thin film deposited via green sol–gel route. *J. Mater. Res. Technol.* **2019**, *8*, 1434–1439. [CrossRef]
95. Mohammadi, M.R.; Fray, D.J.; Mohammadi, A. Sol–gel nanostructured titanium dioxide: Controlling the crystal structure, crystallite size, phase transformation, packing and ordering. *Microporous Mesoporous Mater.* **2008**, *112*, 392–402. [CrossRef]
96. Mohammadi, M.R.; Cordero-Cabrera, M.C.; Fray, D.J.; Ghorbani, M. Preparation of high surface area titania (TiO_2) films and powders using particulate sol–gel route aided by polymeric fugitive agents. *Sens. Actuators B Chem.* **2006**, *120*, 86–95. [CrossRef]
97. Lim, C.S.; Ryu, J.H.; Kim, D.-H.; Cho, S.-Y.; Oh, W.-C. Reaction morphology and the effect of pH on the preparation of TiO_2 nanoparticles by a sol-gel method. *J. Ceram. Process. Res.* **2010**, *11*, 736–741.
98. Javed, A.H.; Shahzad, N.; Khan, M.A.; Ayub, M.; Iqbal, N.; Hassan, M.; Hussain, N.; Rameel, M.I.; Shahzad, M.I. Effect of ZnO nanostructures on the performance of dye sensitized solar cells. *Sol. Energy* **2021**, *230*, 492–500. [CrossRef]